DOI 10.1007/s10946-024-10219-0
Journal of Russian Laser Research, Volume 45, Number 3, May, 2024

PROPAGATION PROPERTIES OF PARTIALLY COHERENT VORTEX BEAMS WITH TWIST PHASE IN OCEANIC TURBULENCE

NianChi Hao, Yonggen Xu,* Qian Xu, Wenli Liu, Bangzhuo An, Xueru Deng, and Zairu Ma

Department of Physics, Key Laboratory of High-Performance Scientific Computation School of Science, Xihua University Chengdu 610039, China

*Corresponding author e-mail: xuyonggen06@126.com

Abstract

We derive the analytical expressions of the average intensity of a partially coherent twisted Laguerre–Gaussian vortex (PCTLGV) beam passing through oceanic turbulence with the help of the extended Huygens–Fresnel principle. The findings show that the normalized initial profile with a dark hollow distribution of PCTLGV beam gradually converts into a flat-topped one, and finally degenerates into a Gaussian-like distribution as the propagation distance increases. The outcomes also reveal that the effect of oceanic turbulence on the propagation properties of PCTLGV beam can be effectively mitigated by regulating the twist factor and topological charge. We also find that PCTLGV beam exhibits stronger anti-turbulence ability, when the topological charge and twist factor have opposite signs as well as larger absolute values of twist factor. In addition, the PCTLGV beam will degenerate fast in stronger turbulence over the poor turbulence, which can be counteracted by increasing the initial coherence lengths. Our researches can contribute to underwater communication transmission, oceanic laser radar detection, and optical imaging.

Keywords: PCTLGV beam, oceanic turbulence, average intensity.

1. Introduction

In recent years, with the increasing frequency of activities, submarine landform surveying, and marine science monitoring, the demand for high-capacity, high-speed, and high-fidelity underwater communication has become increasingly urgent. In daily life, underwater communication mainly includes acoustic communication, underwater radio frequency communication, and underwater wireless optical communication. Acoustic and RF communications have low modulation bandwidths, resulting in low transmission rates, short distances, and communication delays [1–6]. In contrast, underwater wireless optical communication has advantages such as high transmission rates, good confidentiality, and low delay; it has attracted great attention from researchers in recent years [1, 3, 7, 8]. At the intersection of different water currents, the vortices of different sizes and velocities are formed [9–14]. The energy of these eddies is transferred from large-scale eddies to small-scale eddies, and small-scale eddies are formed by the fragmentation and decomposition of large-scale eddies. These eddies are constantly generated, then become smaller, and finally disappear, causing interactions between different motions and forming random ocean currents known as ocean turbulence [15–22]. The stable temperature-salinity field is perturbed by the

Manuscript submitted by the authors in English on February 17, 2024.

 1071-2836/24/4503-0332

velocity field, resulting in random changes in the refractive index of seawater, which leads to random changes in the wavefront during the transmission of light beams. As a result, light beams experience a number of turbulence effects, including intensity fluctuations, beam scattering, and drift [21–26]. Compared with the more popular research on atmospheric turbulence optical communication in recent years, the influence factors are more complicated with oceanic turbulence. For example, the factors affecting atmospheric turbulence are temperature, pressure, and the generalized refractive structure constant of the air, etc. The size of the oceanic turbulence is mainly determined by factors such as the relative strength of temperature and salinity fluctuations, the kinetic energy dissipation rate, the rate of dissipation of mean-square temperature, etc. Therefore, the spatial power spectrum of the refractive-index fluctuations of the turbulence used during the calculation process is also different [13, 14, 26–29].

In recent years, researchers have found that beams can generate excellent anti-turbulence characteristics by modulating the phase function, coherence, and polarization structure [28–31]. Researchers have found that partially coherent beams have better propagation characteristics compared to fully coherent beams [32, 33]. In 2003, T. Shirai explained the reason by using the coherent mode representation of the beam [34]. Due to the unique properties of helical wavefront structures, vortex beams have shown excellent application prospects in fields such as optical tweezers and particle manipulation [27, 35–37]. In addition, vortex beams with orbital angular momentum (OAM) can be used as information carrier, which can increase the information capacity of transmission and improve the confidentiality of communication [38, 39]. The twist phase, as the unique phase of partially coherent light beams, was originally introduced by Simon [40]. It is represented as $\exp[ik\mu(x_1y_2 - x_2y_1)]$, where μ is the twisted factor. Many studies have shown that the beams carrying the twisted phase have greater advantages in resisting the beam drift and intensity scintillation caused by turbulence [41–47].

Up to now, to the best of our knowledge, the propagation properties of a partially coherent twisted Laguerre–Gaussian vortex (PCTLGV) beam passing through oceanic turbulence have not been explored. Therefore, in this paper, we investigate the normalized average intensity of PCTLGV beam in oceanic turbulence. We discuss in details the effects of the rate of dissipation of mean-square temperature, kinetic energy dissipation rate, twisted factor, topological charge, initial correlation length, and beam order on average intensity distribution for the PCTLGV beam.

2. Theory

Based on the unified theory of coherence and polarization, the second-order correlation properties of a PCTLGV beam in source plane can be characterized by a 2×2 cross-spectral density (CSD) matrix [26, 28, 30]; it reads

$$\mathbf{W}(\mathbf{r}_1', \mathbf{r}_2'; z) = \begin{bmatrix} W_{xx}(\mathbf{r}_1', \mathbf{r}_2'; z) & W_{xy}(\mathbf{r}_1', \mathbf{r}_2'; z) \\ W_{yx}(\mathbf{r}_1', \mathbf{r}_2'; z) & W_{yy}(\mathbf{r}_1', \mathbf{r}_2'; z) \end{bmatrix}, \tag{1}$$

where $\mathbf{r}_1' = (x_1', y_1')$ and $\mathbf{r}_2' = (x_2', y_2')$ are positions of two points at the source plane $z = 0$.

The elements of CSD matrix in Eq. (1) $W_{\alpha\beta}(\mathbf{r}'_1, \mathbf{r}'_2; z=0)$ can be expressed as follows [29,31]:

$$W_{\alpha\beta}(x'_1, y'_1, x'_2, y'_2; 0) = \frac{1}{2^{4n+2m}(n!)^2} \cdot \exp\left(-\frac{x'^2_1 + y'^2_1 + x'^2_2 + y'^2_2}{w_0^2}\right) \cdot \exp\left[-\frac{(x'_1 - x'_2)^2 + (y'_1 - y'_2)^2}{2\delta^2_{\alpha\beta}}\right]$$
$$\times \sum_{t=0}^{n}\sum_{s=0}^{m}\sum_{\gamma=0}^{n}\sum_{\nu=0}^{m}(i^s)^* i^\nu \binom{n}{t}\binom{m}{s}\binom{n}{\gamma}\binom{m}{\nu} H_{2t+m-s}\left(\frac{x'_1}{a_0}\right) H_{2\gamma+m-\nu}\left(\frac{x'_2}{a_0}\right)$$
$$\times H_{2n-2t+s}\left(\frac{y'_1}{a_0}\right) H_{2n-2\gamma+\nu}\left(\frac{y'_2}{a_0}\right) \exp\left[-ik\mu(x'_1 y'_2 - x'_2 y'_1)\right], \quad (2)$$

where μ is the twisted factor, and w_0 represents the waist of the fundamental Gaussian beam, the variables m and n denote the topological charge number and the beam order, respectively, $\delta_{\alpha\beta}$ ($\alpha = x, y$, $\beta = x, y$) are initial auto-correlation lengths for convenience, and $k = 2\pi/\lambda$ is the wave number, with λ being the wavelength. We set $\delta_{xx} = \delta_{yy} = \delta_1$. Also, $a_0 = w_0/\sqrt{2}$, $H(\cdot)$ represents the Hermite polynomial, and $\binom{n}{p}$ and $\binom{m}{q}$ are the binomial coefficients, with $p = t$, γ, and $q = s$, v.

Subsequently, in view of the extended Huygens–Fresnel principle, the cross-spectral density function, which describes the effect of oceanic turbulence on the receiving surface, can be expressed as follows [36, 37]:

$$W_{\alpha\beta}(\mathbf{r}_1, \mathbf{r}_2; z) = \frac{1}{\lambda^2 z^2} \iiiint W_{\alpha\beta}(x'_1, y'_1, x'_2, y'_2; 0) \cdot \langle \exp[\Psi_1 + \Psi_2^*] \rangle$$
$$\times \exp\left\{-\frac{ik}{2z}\left[(x'_1 - x_1)^2 - (y'_1 - y_1)^2\right]\right\} \exp\left\{-\frac{ik}{2z}\left[(x'_2 - x_2)^2 - (y'_2 - y_2)^2\right]\right\} dx'_1 dy'_1 dx'_2 dy'_2, \quad (3)$$

where $\mathbf{r}_1 = (x_1, y_1)$ and $\mathbf{r}_2 = (x_2, y_2)$ are the coordinates of any two points in the receiving plane, the $\langle\cdot\rangle$ represents the ensemble average, asterisk $*$ denotes the complex conjugate, $\Psi(\cdot)$ signifies the random part of the complex phase of a spherical wave due to the existence of the turbulence, whose ensemble average of the turbulent ocean reads

$$\langle \exp[\Psi_1 + \Psi_2^*] \rangle = \exp\left[-\frac{1}{r_0^2}(\mathbf{r}'^2_d + \mathbf{r}'_d \cdot \mathbf{r}_d + \mathbf{r}_d^2)\right], \quad (4)$$

where $\mathbf{r}'_d = (x'_1 - x'_2, y'_1 - y'_2)$, $\mathbf{r}_d = (x_1 - x_2, y_1 - y_2)$, and r_0 is the spatial coherence length of spherical wave propagation in the turbulence, which is

$$r_0 = \left[\frac{1}{3}\pi^2 k^2 z \int_0^\infty \Phi_n(\varkappa)\varkappa^3 \, d\varkappa\right]^{-1/2}, \quad (5)$$

with $\Phi_n(\varkappa)$ being the spatial power spectrum of the refractive-index fluctuations of the turbulent ocean. Based on the Markov approximation, the spatial power spectrum model of isotropic oceanic turbulence can be written as [25, 26]

$$\Phi_n(\varkappa) = 0.388 \cdot 10^{-8} \varepsilon^{-1/3} \chi_T \varkappa^{-11/3}(1 + 2.35\varkappa^{2/3}\eta^{2/3})$$
$$\times \left[\exp(-A_T\delta) + \omega^{-2}\exp(-A_S\delta) - 2\omega^{-1}\exp(-A_{TS}\delta)\right], \quad (6)$$

where $A_T = 1.863 \cdot 10^{-2}$, $A_S = 1.9 \cdot 10^{-4}$, $A_{TS} = 9.41 \cdot 10^{-3}$, $\delta = 8.284(\varkappa\eta)^{4/3} + 12.978(\varkappa\eta)^2$, ε represents the kinetic energy dissipation rate, χ_T denotes rate of dissipation of mean-square temperature of oceanic turbulence, ω signifies the relative strength of temperature and salinity fluctuations, and η stands for the internal scale factor of oceanic turbulence. The range of values for ε is between 10^{-10} and 10^{-1} ($\mathrm{m}^2/\mathrm{s}^3$); for χ_T, it is between 10^{-10} and 10^{-4} (K^2/s), and, for ω, it falls within the range of $[-5, 0]$. When $\omega = -1$, it indicates predominantly salinity-induced optical turbulence, and when $\omega = -5$, it represents temperature-induced optical turbulence. Substituting Eq. (6) into Eq. (5), we can obtain the lateral coherence length of the spherical wave in the oceanic turbulence [14, 18]; it reads

$$r_0 = \left[1.2765 \cdot 10^{-8} k^2 z \omega^{-2} (\varepsilon\eta)^{-1/3} \chi_T (6.78335\omega^2 - 17.6701\omega + 47.5708)\right]^{-1/2}. \tag{7}$$

Substituting Eqs. (2) and (4) into Eq. (3), and obtain the following the analytical formulas for CSD of the PCTLGV beam propagating through oceanic turbulence:

$$\begin{aligned} W_{\alpha\beta}(x_1, y_1, x_2, y_2; z) = {} & \frac{k^2\pi^2 (i^s)^* i^\nu}{2^{4n+2m}(2\pi z n!)^2} \exp\left[-\frac{ik}{2z}(r_1^2 - r_2^2) - \frac{1}{r_0^2}(r_1 - r_2)^2\right] \\ \times \sum_{t=0}^{n}\sum_{s=0}^{m}\sum_{\gamma=0}^{n}\sum_{\nu=0}^{m}\sum_{a=0}^{a_1}\sum_{b=0}^{a_2}\sum_{c=0}^{a_3}\sum_{d=0}^{a_4}\sum_{e=0}^{a_5}\sum_{f=0}^{a_6}\sum_{g=0}^{a_7}\sum_{\gamma=0}^{a_8}\sum_{j=0}^{a_9}\sum_{l=0}^{a_{10}}\sum_{w=0}^{a_{11}}\sum_{p=0}^{a_{12}}\sum_{q=0}^{a_{13}} & \binom{n}{t}\binom{m}{s}\binom{n}{\gamma}\binom{m}{\nu} \\ \binom{e}{f}\binom{a_1}{a}\binom{a_2}{b}\binom{a_9}{j}\binom{a_5}{e} & D_1 \sqrt{2}^{b_1} (i)^{b_2} (k\mu)^{b_3} \left(\frac{1}{\sqrt{A_1}}\right)^{b_5} \left(\frac{1}{\sqrt{A_1^2 w_0^2/(2 - A_1)}}\right)^{b_6} \\ \times A_2^{b_1} C_4^{b_8} \left(\frac{1}{\sqrt{C_1}}\right)^{b_9} \left(\frac{1}{\sqrt{C_3}}\right)^{b_{10}} \left(\frac{1}{\sqrt{C_6}}\right)^{b_{11}} & \exp\left(\frac{B_{1x}^2}{4A_1} + \frac{C_2^2}{4C_1} + \frac{C_5^2}{4C_3} + \frac{G^2}{4C_6}\right) \\ H_{d1}\left(\frac{B_{1x}\sqrt{2}}{\sqrt{A_1 a_0^2 - A_1}}\right) H_{d2}\left(\frac{iC_2\sqrt{2}}{2\sqrt{C_1}}\right) H_{d3}\left(\frac{iC_5\sqrt{2}}{2\sqrt{C_3}}\right) H_{d4}\left(\frac{iG}{2\sqrt{C_6}}\right), \end{aligned} \tag{8}$$

with

$$\begin{aligned} A_1 &= \frac{1}{w_0^2} + \frac{1}{2\delta_1^2} + \frac{ik}{2z} + \frac{1}{r_0^2}, \quad A_2 = \frac{1}{\delta_1^2} + \frac{2}{r_0^2}, \quad B_{1x} = \frac{ikx_1}{z} - \frac{x_1 - x_2}{r_0^2}, \quad B_{1y} = \frac{iky_1}{z} - \frac{y_1 - y_2}{r_0^2}, \\ B_{2x} &= -\frac{ikx_2}{z} + \frac{x_1 - x_2}{r_0^2}, \quad B_{2y} = -\frac{iky_2}{z} + \frac{y_1 - y_2}{r_0^2}, \quad C_1 = -\frac{A_2^2}{4A_1} + A_1^*, \quad C_2 = \frac{A_2 B_{1x}}{2A_1} + B_{2x}, \\ C_3 &= \frac{k^2\mu^2}{4C_1} + A_1, \qquad C_4 = \frac{k^2\mu^2 A_2}{4A_1 C_1} + A_2, \qquad C_5 = \frac{ik\mu C_2}{2C_1} + B_{1y}, \\ C_6 &= \frac{k^2\mu^2}{4A_1} + \frac{k^2\mu^2 A_2^2}{16A_1^2 C_1} - \frac{C_4^2}{4C_3} + A_1^*, \qquad G = -\frac{ik\mu B_{1x}}{2A_1} - \frac{ikA_2 C_2 \mu}{4A_1 C_1} + \frac{C_4 C_5}{2C_3} + B_{2y} \end{aligned} \tag{9}$$

and

$$a_1 = 2t + m - s, \qquad a_2 = 2t + m - s - a, \qquad a_3 = \frac{a}{2}, \qquad a_4 = \frac{2\gamma + m - \nu}{2},$$
$$a_5 = 2\gamma + m - \nu + a - 2c - 2d, \qquad a_6 = e, \qquad a_7 = \frac{f}{2}, \qquad a_8 = \frac{2n - 2t + s}{2},$$
$$a_9 = 2n - 2t + s + f - 2g - 2h, \qquad a_{10} = \frac{b}{2}, \qquad a_{11} = \frac{e - f}{2}, \qquad a_{12} = \frac{j}{2}, \qquad a_{13} = \frac{2n - 2\gamma + \nu}{2},$$
$$b_1 = a + 4c + 2d - 3e + f + 2g + 2h - j + 2l - 3m - 2n + 2p + s - 2t - 2\gamma + \nu + 4w,$$
$$b_2 = -a + 2c + 2d - e + 2g + 2h - m - 4n + 2q - s + 2t + 2w, \qquad b_3 = b + e - 2g - 2l - 2w,$$
$$b_4 = 2m + 4n - 2d - 2h - 2q, \qquad b_5 = 2m - 2s + 4t + 2e - 2f - 4w + 1,$$
$$b_6 = a + b - 2c - 2l - m + s - 2t, \qquad b_7 = a - 2c + e - f - 2w, \qquad b_8 = j - 2p,$$
$$b_9 = a - 2c - 2d + e - 2g + m + 2\gamma - \nu - 2w + 1, \qquad b_{10} = f - 2g - 2h + j + 2n - 2t + s - 2p + 1,$$
$$b_{11} = b + e - f + j - 2l + 2n - 2p - 2q - 2\gamma + \nu - 2w + 1, \qquad d_1 = 2t + m - s - a - b,$$
$$d_2 = a - 2c - 2d - e + 2\gamma + m - \nu, \qquad d_3 = f - 2g - 2h - j + 2n - 2t + s,$$
$$d_4 = b + e - f + j - 2l + 2n - 2p - 2q - 2\gamma + \nu - 2w,$$
$$D_1 = \frac{(-1)^{b+c+d+f-g+h-l+p+q+w} a!b!f!j!}{c!d!g!h!l!p!q!w!(a-2c)!(b-2l)!(f-2g)!(j-2p)!}(2n - 2\gamma + \nu - 2q)!(2\gamma + m - \nu - 2d)!$$
$$\times \frac{(e-f)!(2n-2t+s)!(2n-2\gamma+\nu)!(2\gamma+m-\nu)!}{(e-f-2w)!(2n-2t+s-2h)!(2n-2\gamma+\nu-2q)!(2\gamma+m-\nu-2d)!}. \quad (10)$$

In Eqs. (8)–(10), the average intensity of PCTLGV beam in the receiving plane can be obtained by setting $x_1 = x_2 = x$ and $y_1 = y_2 = y$ in Eq. (8); finally, we arrive at

$$I(x, y; z) = W_{xx}(x, y; z) + W_{yy}(x, y; z). \quad (11)$$

Applying the above-derived formulas, the average intensity of PCTLGV beam propagating through oceanic turbulence can be directly investigated. We can find from Eqs. (8)–(10) that average intensity is determined by the beam parameters w_0, δ_1, λ, μ, m, and n and the turbulence parameters χ_T, ε, and ω.

3. Numerical Examples and Discussions

Here, we study the numerical results of the average intensity for PCTLGV beam in oceanic turbulence under different beam parameters and turbulence parameters.

From Fig. 1, we obtain that the intensity distribution of PCTLGV beam is influenced by oceanic turbulence. In Fig. 1 a, b, we show that the PCTLGV beam propagating through the turbulent ocean for a short distance ($z \leq 50$ m) can maintain multi-ring dark hollow structure, where the number of the dark rings is 2. When 50 m $\leq z \leq$ 500 m, in Fig. 1 c–e, we see that with increase in the propagation distance, the intensity of the dark center region gradually increases. As the dark ring gradually disappears, the outer ring with the lowest intensity gradually increases. Then the dark hollow structure both inside and outside gradually disappears, and the beam finally evolves into semi-hollow beam. With a further increase in the propagation distance ($z \geq 500$ m), the evolution speed of the beam in the ocean turbulence obviously increases, and the beam profile tends to the Gaussian-like distribution; see Fig. 1 e, f. This is consistent with the conclusion in [26]. We conclude that the random ocean turbulence destroys the initial

structure of the beam with the accumulation of the propagation distance, and the normalized intensity eventually evolves into Gaussian-like distribution.

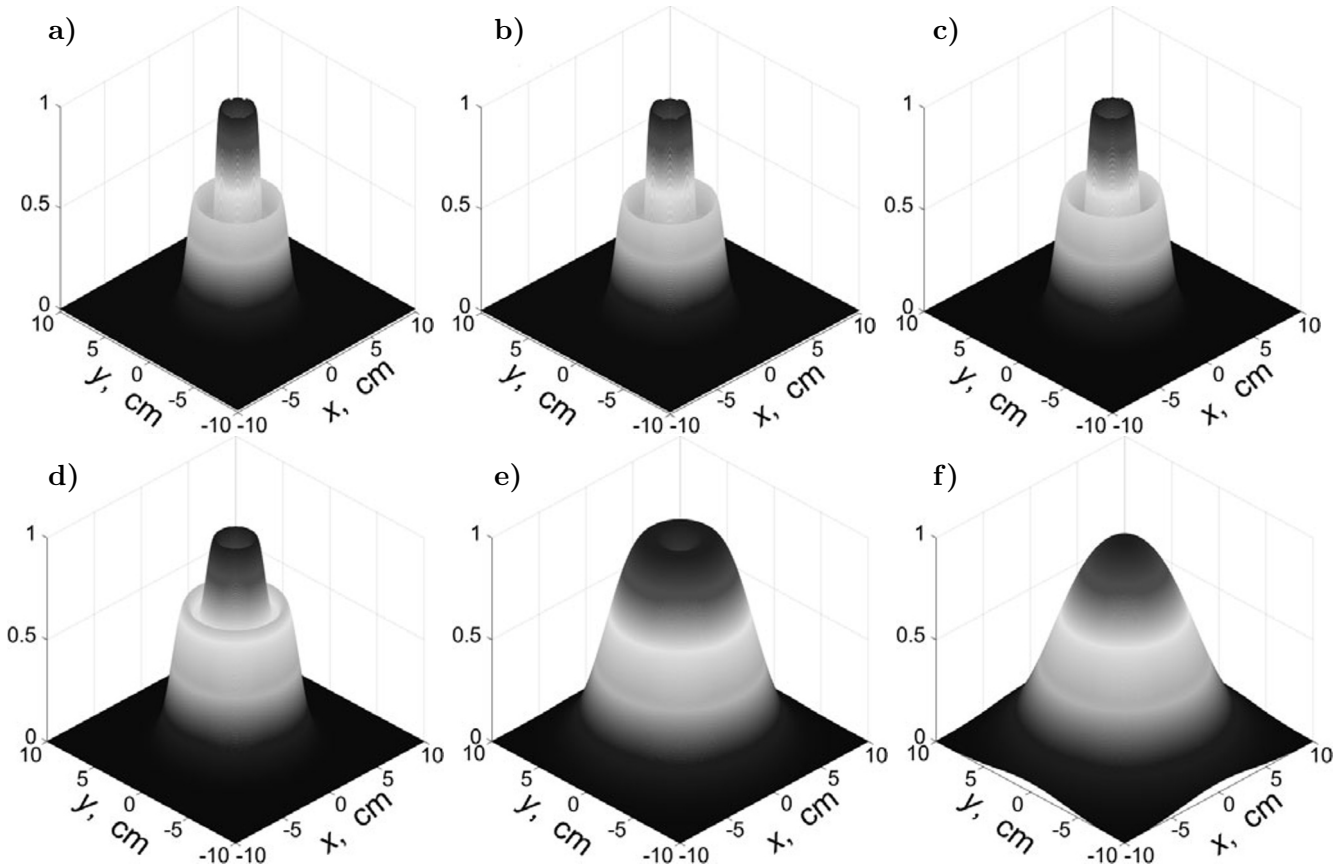

Fig. 1. The normalized average intensity distribution of PCTLGV beam with $z = 0$ (a), $z = 50$ m (b), $z = 200$ m (c), $z = 350$ m (d), $z = 500$ m (e), and $z = 900$ m (f) in ocean turbulence. Calculation parameters are $n = 1$, $m = 2$, $\mu = -1 \cdot 10^{-3}$ m^{-1}, $\lambda = 632.8$ nm, $\delta_1 = 10$ mm, $w_0 = 20$ mm, $\varepsilon = 10^{-5}$ m^2/s^3, $\chi_T = 4 \cdot 10^{-7}$ k^2/s, and $\omega = -3$.

Figure 2 portrays the normalized intensity distribution of the PCTLGV beam under different m and μ in ocean turbulence. When $m = 0$, the beam descends into a partially coherent twisted beam; at this time, the normalized intensity appears a Gaussian-like distribution, while the alteration in μ having a negligible impact on it; see Fig. 2 a1–a5. In the case of adding vortex phase to the partially coherent twisted light, the beam becomes PCTLGV beam and disrupts the Gaussian-like pattern of the light shown in Fig. 2 b–d. At $\mu = 0$, the beam transforms into a partially coherent Laguerre-Gaussian beam (PCLGB). In Fig. 2 b3 for m=1, the beam appears to a nearly flat-topped distribution; as m increasing, the beam progresses into a semi-hollow state, and finally evolves into a hollow state; see refer Fig. 2 b3–d3. The result shows that with increase in m, the beam has a higher hollow degree and stronger anti-turbulence ability. In addition, the normalized intensity of the PCTLGV beam depends on the interplay between m and μ. The observed phenomenon suggests that a positive twisted factor expedites the beam degradation process towards a Gaussian beam, while this degradation process is inhibited under a negative twisted factor. In instances where the sign of m opposes that of μ, a larger $|\mu|$ equates to a stronger ability to maintain

a hollow configuration. In contrast, when the signs of m and μ align, a smaller $|\mu|$ results in a stronger ability to maintain a hollow configuration. Our studies reveal that the emergence of this phenomenon can be attributed to the inherent orbital angular momentum in both parameters, m and μ. If their chirality is consistent (with opposite sign), the orbital angular momentum undergoes superposition. In contrast, if their chirality differs (with same sign), the orbital angular momentum is canceled [29].

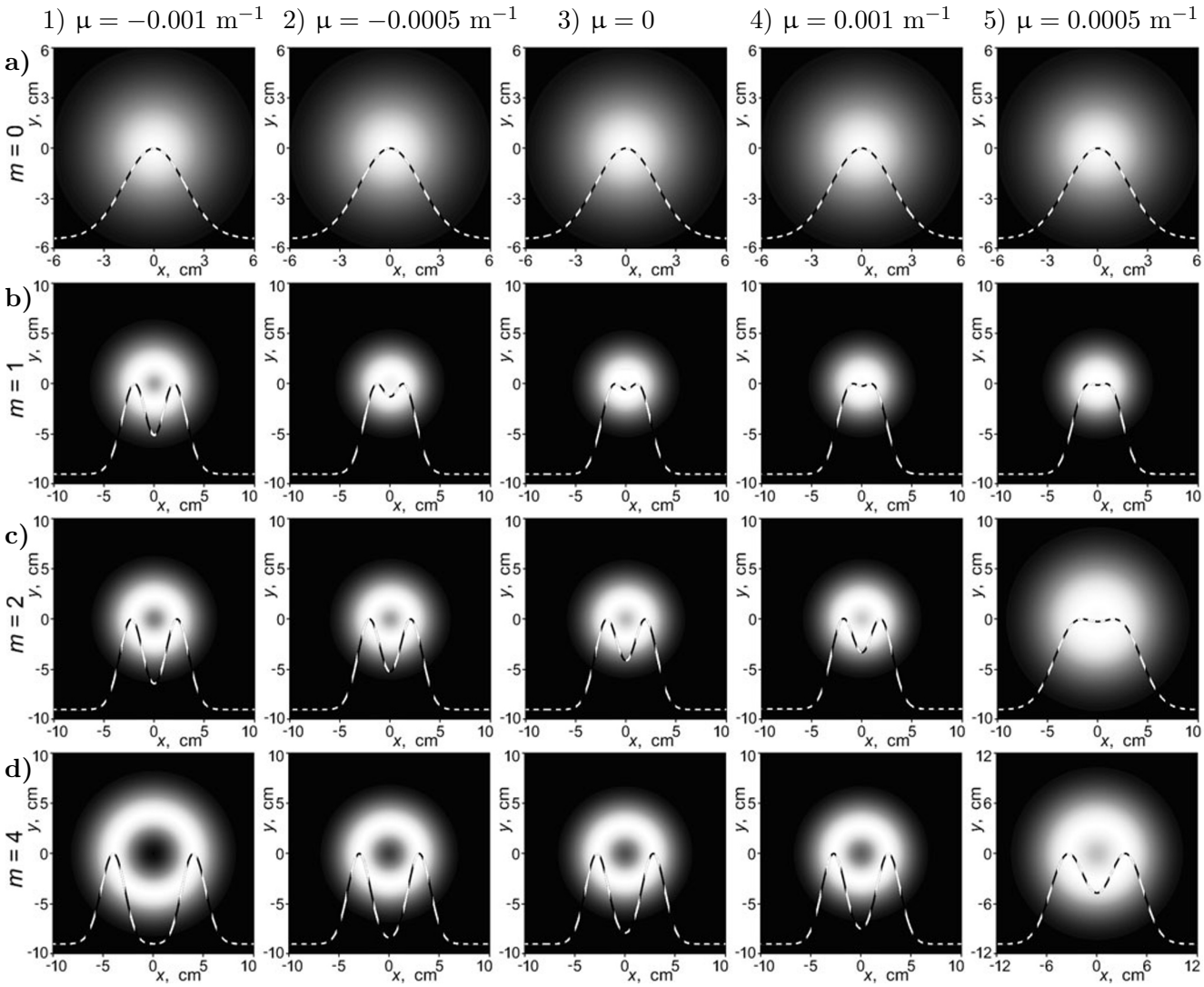

Fig. 2. The normalized average intensity distribution of PCTLGV beam with different μ and m in ocean turbulence. Calculation parameters are $z = 400$ m, $n = 0$, $\lambda = 632.8$ nm, $\delta_1 = 10$ mm, $w_0 = 20$ mm, $\varepsilon = 10^{-5}$ m^2/s^3, $\chi_T = 4 \cdot 10^{-7}$ k^2/s, and $\omega = -3$.

With the help of Fig. 3, we investigate the variation of normalized optical intensity with transmission distance and kinetic dissipation rate, and study the impact of the initial coherence length on the beam intensity distribution, when z and χ_T are fixed. As shown in Fig. 3, regardless of the changing values of χ_T, the normalized optical intensity of PCTLGV beam gradually augments with increase in the transmission distance. The inner and outer dark rings grow, transforming the hollow beam into a semi-hollow one and

eventually evolving into a Gaussian-like beam. In Fig. 3 b1–b3, it is evident that the initial coherence length also affects the intensity distribution. In Fig. 3 b1, when $\delta_1 = 10$ mm, the beam exhibits a hollow structure with two dark rings; when $\delta_1 = 1$ mm, the beam shows a semi-hollow structure with two dark rings, and when $\delta_1 = 0.5$ mm, the inner dark ring completely disappears, and the outer dark ring partially vanishes, resulting in a beam with a Gaussian-like distribution. It can be inferred that a larger δ_1 enhances the capability of maintaining a double dark ring hollow structure, while a smaller δ_1 makes the beam more prone to degrade into a Gaussian-like beam. Furthermore, in Fig. 3 a2–c2, we can observe that, with increase in χ_T, the rate, at which the beam degrades into a Gaussian-like beam intensifies, leads to a more severe disruption of the beam structure.

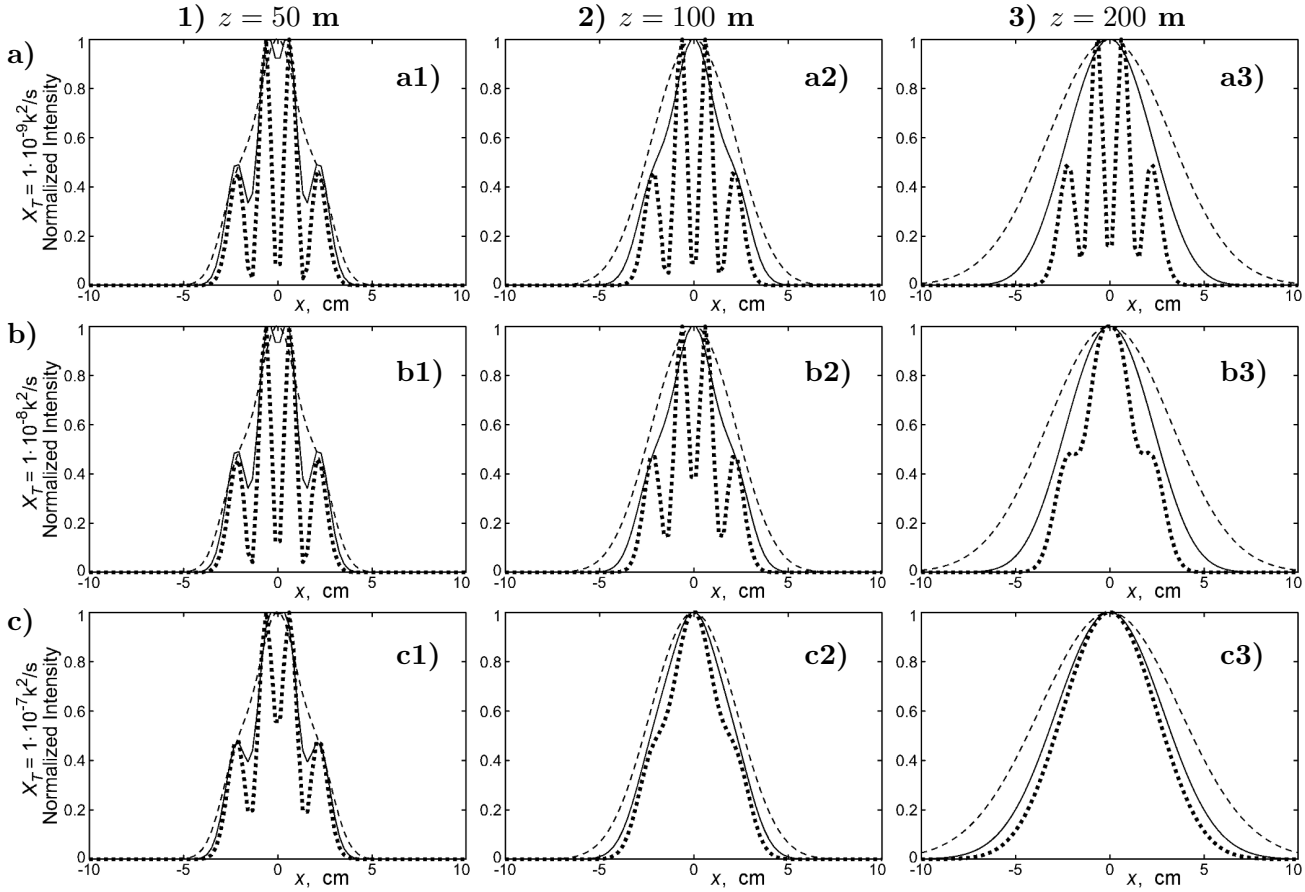

Fig. 3. The normalized average intensity distribution of PCTLGV beam with different z, δ_1, and χ_T in ocean turbulence. Calculation parameters are $m = 2$, $n = 1$, $\lambda = 632.8$ nm, $w_0 = 20$ mm, $\varepsilon = 10^{-5}$ m^2/s^3, $\omega = -3$, and $\mu = -1 \cdot 10^{-3}$ m^{-1}, with $\delta_1 = 0.5$ mm (dashed curves), $\delta_1 = 1$ mm (solid curves), and $\delta_1 = 10$ mm (dotted curves). Here, $z = 50$ m (the left panel), $z = 100$ m (the middle panel), and $z = 200$ m(the right panel).

In Fig. 4, we display the normalized intensity of PCTLGV beam at several different propagation distances in oceanic turbulence for different values ε. The conclusions that PCTLGV beam entirely evolves into Gaussian-like beam from ring hollow dark distribution and the light spot is larger with increase in transmission distances are consisted with before. When $z = 60$ m, with decrease of ε, the beam gradually evolves from a hollow beam to a flat-topped beam; see Fig. 4 a1–c1. When 60 m $< z <$ 120 m,

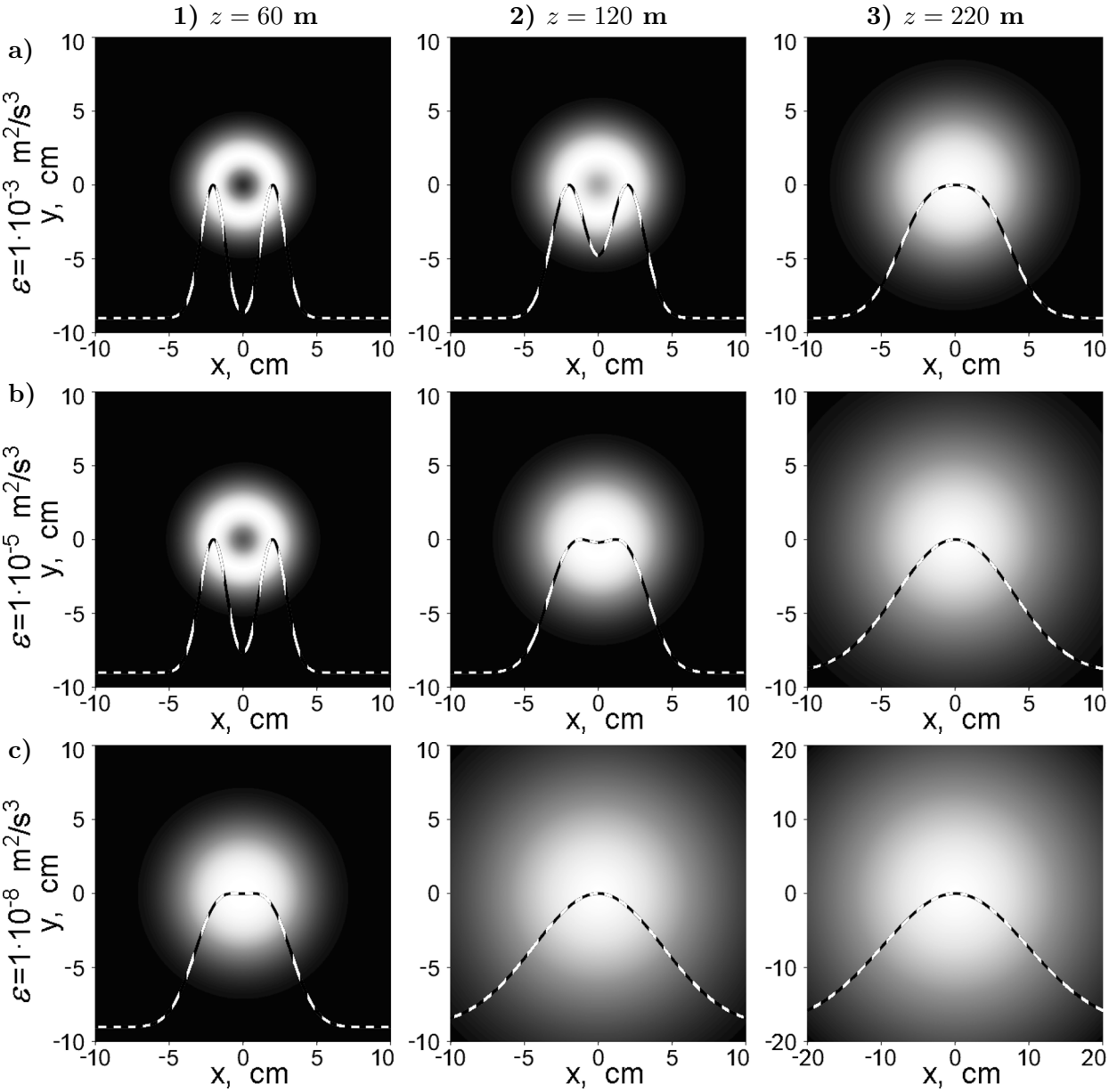

Fig. 4. The normalized average intensity distribution of PCTLGV beam with different ε and z in ocean turbulence. Calculation parameters are $n = 0$, $m = 1$, $\lambda = 632.8$ nm, $\delta_{xx} = \delta_{yy} = 2$ mm, $w_0 = 20$ mm, $\chi_T = 4 \cdot 10^{-7}$ k^2/s, $\omega = -3$, and $\mu = -1 \cdot 10^{-3}$ m^{-1}. Here, $z = 60$ m (the left panel), $z = 120$ m (the middle panel), and $z = 220$ m(the right panel).

the beam gradually transforms from a hollow beam to a semi-hollow beam in Fig. 4 a1, a2, evolves from a semi-hollow beam to a flat-topped beam in Fig. 4 b1, b2, and further evolves from a flat-topped beam to a Gaussian-like beam in Fig. 4 c1, 2. This phenomenon indicates that as ε decreases, there is smaller conversion of the turbulent kinetic energy into the molecular thermal motion energy. At this point, the impact of ocean turbulence on the PCTLGV beam increases. If 120 m$< z <$ 220 m, the beams gradually

evolve into Gaussian-like beams; see Fig. 4 c1–c3. Hence, it can be inferred that, when being transmitted in ocean turbulence with larger ε, the beam exhibits better transmission characteristics.

4. Conclusions

In conclusions, we derived the analytical formulas for the CSD matrix elements of PCTLGV beam propagating through oceanic turbulence by employing the extended Huygens–Fresnel principle. Meanwhile, we carried out the numerical calculations of PCTLGV beam and demonstrated the correctness and validity of analytical expressions. The results obtained indicate that with increase in transmission distance and the cumulative disruption of the beam phase by ocean turbulence, PCTLGV beam evolves from a hollow beam into a Gaussian-like beam. Additionally, the beam is influenced by the joint regulation of m and μ. In instances, where the sign of m opposes that of μ, a larger $|\mu|$ equates to a stronger ability to maintain a hollow configuration. In contrast, when the signs of m and μ align, a smaller $|\mu|$ results in a stronger ability to maintain a hollow configuration. Additionally, our study found that rate of dissipation of mean-square temperature and kinetic energy dissipation rate had a notable impact on the intensity distribution of PCTLGV beam. When the rate of dissipation of mean-square temperature is higher and the kinetic energy dissipation rate is lower, the turbulence effect on the beam becomes more pronounced. Consequently, it is possible to enhance the beam's turbulence resistance by increasing the initial coherence length. Our numerical findings may have a great significance for detection and imaging of the oceanic optical telecommunication links.

Acknowledgments

This work is supported by the Yunnan Key Laboratory of Solar Physics and Space Science under Grant No. YNSPCC202202, the National Natural Science Foundation of China (NSFC) under Grant No. 11703011, the Department of Science and Technology of Sichuan Province under Grant No. 2019YJ0470, and the Sichuan Provincial University Key Laboratory of Detection and Application of Space Effect in Southwest Sichuan under Grant No. ZDXM202201003.

References

1. S. Z. Liu, G. Qiao, and Y. L. Yin, *Acta. Phys. Sin.*, **62**, 144303 (2013).
2. M. F. Ali, D. N. K. Jayakody, and Y. Li, *IEEE Access*, **10**, 22169 (2022).
3. Y. R. Niu, X. Yan, J. X. Chen, et al., *Infrared Phys. Technol.*, **125**, 104243 (2022).
4. R. X. Liu and L. Ma, *Acta. Phys. Sin.*, **71**, 010304 (2022).
5. F. T. He, Y. Du, J. L. Zhang, et al., *Acta Phys. Sin.*, **68**, 164206 (2019).
6. X. J. Li, L. M. Sun, J. M. Huang, et al., *J. Mar. Sci. Eng.*, **11**, 341 (2023).
7. Q. Zhang, D. W. Yue, and X. Y. Xu, *Opt. Express.*, **31**, 37943 (2023).
8. H. C. Qiu, Z. T. Huang, J. Xu, et al., *Opt. Lett.*, **48**, 636 (2023).
9. A. E. Gargett, *Annu. Rev. Fluid Mech.*, **21**, 419 (1989).
10. O. Korotkova, N. Farwell, and E. Shchepakina, *Waves Random Complex Media*, **22**, 260 (2012).
11. X. Yi, Z. Li, Z. and J. Liu, *Appl. Opt.*, **54**, 1273 (2015).
12. W. Wen, Z. B. Wang, and C. H. Qiao, *Optik*, **252**, 168428 (2022).
13. H. C. Zhan, B. Chen, Y. X. Peng, et al., *Chin. Phys. B.*, **32**, 044208 (2023).
14. Y. Q. Pan, M. L. Zhao, M. M. Zhang, et al., *Opt. Laser Technol.*, **159**, 109024 (2023).

15. J. R. Taylor and A. F. Thompson, *Annu. Rev. Fluid Mech.*, **55**, 103 (2023).
16. Z. Su, J. B. Wang, P. Klein, et al., *Nat. Commun.*, **9**, 775 (2018).
17. I. Frenger, N. Gruber, R. Knutti, et al., *Nat. Geosci.*, **6**, 608 (2013).
18. J. R. Yao, H. T. Wang, H. J. Zhang, et al., *Opt. Express*, **29**, 1340 (2021).
19. L. I. Piterbarg, *SIAM J. Appl. Math.*, **62**, 777 (2002).
20. M. H. Alford and R. Pinkel, *J. Phys. Oceanogr.*, **30**, 805 (2000).
21. V. M. Canuto, A. Howard, Y. Cheng, et al., *J. Phys. Oceanogr.*, **32**, 240 (2002).
22. H. Seo, L. W. O'Neill, M. A. Bourassa, et al., *J. Clim.*, **36**, 1981 (2023).
23. C. Sun, X. Lv, B. B. Ma, et al., *Opt. Express.*, **27**, A245 (2019).
24. F. Ye, J. Zhang, J. T. Xie, et al., *Opt. Commun.*, **426**, 456 (2018).
25. V. V. Nikishov and V. I. Nikishov, *Int. J. Fluid Mech. Res.*, **27**, 82 (2000).
26. Y. G. Xu, Q. Xu, W. L. Liu, *J. Opt. Soc. Am. A*, **40**, 1895 (2023).
27. L. Zhao, Y. G. Xu, and Y. Q. Dan, *Opt. Express*, **29**, 34986 (2021).
28. Y. G. Xu, Y. Q. Dan, and B. Zhang, *Optik*, **127**, 4590 (2016).
29. Y. Xu, L. Zhao, N. Yang, et al., *J. Mod. Opt.*, **69**, 200 (2022).
30. K. Huang, Y. G. Xu, J. Cao, et al., *J. Russ. Laser Res.*, **44**, 110 (2023).
31. Y. P. Huang, Z. C. Duan, X. Y. Huang, et al., *J. Russ. Laser Res.*, **44**, 451 (2023).
32. J. C. Leader, *J. Opt. Soc. Am.*, **66**, 536 (1976).
33. Y. G. Xu, Y. D. Li, and X. L. Zhao, *J. Opt. Soc. Am. A*, **32**, 1623 (2015).
34. T. Shirai, A. Dogariu, and E. Wolf, *J. Opt. Soc. Am. A*, **20**, 1094 (2003).
35. E. Wolf, *J. Opt. Soc. Am.*, **72**, 343 (1982).
36. Q. Xu, Y. G. Xu, L. Zhao, et al., *Phys. Scripta*, **98**, 105504 (2023).
37. B. Z. An, Y. G. Xu, W. L. Liu, et al., *J. Russ. Laser Res.*, **44**, 439 (2023).
38. R. Kumar, D. S. Mehta, A. Sachdeva, et al., *Opt. Commun.*, **281**, 3414 (2008).
39. J. Wang, *Photonics Res.*, **4**, B14 (2016).
40. R. Simon and N. Mukunda, *J. Opt. Soc. Am. A*, **10**, 95 (1993).
41. Y. Q. Zhou, Z. W. Cui, and Y. P. Han, *Opt. Express*, **30**, 23448 (2022).
42. Y. Xu, Y. G. Xu, S. J. Wang, et al., *J. Russ. Laser Res.*, **43**, 509 (2022).
43. F Wang, Y. J. Cai, H. T. Eyyuboglu, et al., *Opt. Lett.*, **37**, 184 (2012).
44. Y. Xu, Y. G. Xu, and T. J. Wang, *Photonics*, **9**, 707 (2022).
45. W. L. Liu, Y. G. Xu, B. Z. An, et al., *J. Russ. Laser Res.*, **44**, 426 (2023).
46. Y. G. Xu, Y. Q. Dan, J. Y. Yu, et al., *J. Mod. Opt.*, **64**, 1976 (2017).
47. C. S. Wang, L. X. Liu, L. Liu, et al., *Opt. Express*, **31**, 13255 (2023).